ADVANCED MATERIALS
www.advmat.de

Superconducting Quantum Metamaterials from Convergence of Soft and Hard Condensed Matter Science

*Peter A. Beaucage, R. Bruce van Dover, Francis J. DiSalvo, Sol M. Gruner, and Ulrich Wiesner**

Superconducting quantum metamaterials are expected to exhibit a variety of novel properties, but have been a major challenge to prepare as a result of the lack of appropriate synthetic routes to high-quality materials. Here, the discovery of synthesis routes to block copolymer (BCP) self-assembly-directed niobium nitrides and carbonitrides is described. The resulting materials exhibit unusual structure retention even at temperatures as high as 1000 °C and resulting critical temperature, T_c, values comparable to their bulk analogues. Applying the concepts of soft matter self-assembly, it is demonstrated that a series of four different BCP-directed mesostructured superconductors are accessible from a single triblock terpolymer. Resulting materials display a mesostructure-dependent T_c without substantial variation of the XRD-measured lattice parameters. Finally, field-dependent magnetization measurements of a sample with double-gyroid morphology show abrupt jumps comparable in overall behavior to flux avalanches. Results suggest a fruitful convergence of soft and hard condensed matter science.

Ordered mesostructures allow access to surprising materials properties that can be very different from their bulk counterparts. For example, mechanical testing has shown remarkable elasticity in brittle ceramic nanolattices,[1] and simulations have suggested the appearance of negative refractive indices in the visible, circularly polarized surface plasmon polariton propagation, and a photonic bandgap in low loss metals with double (space group $Ia\bar{3}d$) and alternating (space group $I4_132$) gyroid structures.[2] Simulations of these and other mesoscale network phases further suggest topologically protected Weyl states[3] and phononic band gaps.[4–6] The manipulation of material symmetry via such superstructures can further open access to properties disallowed by the symmetry of the underlying crystal, for example, "improper" ferroelectricity.[7] This strategy has shown considerable promise in simple superstructures, for example, layers, but has not been substantially expanded to more complex symmetries and structural topologies, for example, the non-centrosymmetric alternating gyroid. Mesostructured superconductors, in particular, are expected to be a fertile area for exploration of the impact of mesoscale order on the properties of correlated electron systems leading to quantum metamaterials. For example, the introduction of simple 1D or 2D ordered porosity can create arrays of artificial flux pinning centers and enhance the critical field, among other properties.[8,9] The expansion of optical metamaterials paradigms to superconducting, 3D ordered phases is further expected to offer unique low-loss and switchable metamaterials.[10,11] However, the exploration of these phenomena is extremely limited by a lack of synthetic strategies to prepare 3D ordered mesostructured superconducting materials.

One promising method to generate such structures is block copolymer self-assembly (BCP SA). BCP SA is a very versatile, tunable technique to produce periodically ordered structures with potentially complex symmetry. The unit cell length scales, typically between 10 nm and 100 nm, can be precisely tailored by varying the BCP molar mass. The method and its theoretical underpinning, traditionally strictly in the realm of soft condensed matter physics, has been extended to produce

Dr. P. A. Beaucage, Prof. R. B. van Dover, Prof. U. Wiesner
Materials Science & Engineering Department
Cornell University
Ithaca, NY 14853, USA
E-mail: ubw1@cornell.edu
Dr. P. A. Beaucage
NIST Center for Neutron Research
National Institute of Standards and Technology
Gaithersburg, MD 20899, USA
Dr. P. A. Beaucage
Materials Science & Engineering Division
National Institute of Standards and Technology
Gaithersburg, MD 20899, USA
The ORCID identification number(s) for the author(s) of this article can be found under https://doi.org/10.1002/adma.202006975.
Prof. F. J. DiSalvo
Chemistry Department
Cornell University
Ithaca, NY 14853, USA
Prof. S. M. Gruner
Physics Department
Cornell University
Ithaca, NY 14853, USA
Prof. S. M. Gruner
Cornell High Energy Synchrotron Source
Cornell University
Ithaca, NY 14853, USA
Prof. S. M. Gruner
Kavli Institute at Cornell for Nanoscale Science
Cornell University
Ithaca, NY 14853, USA

DOI: 10.1002/adma.202006975

functional materials in the form of, for example, oxides,[12–16] semiconductors,[17] metals,[18–20] carbons,[21] and low-T_c superconductors[22] with mesostructure controlled by the parent BCP SA. This convergence of soft and hard condensed matter physics may prove to be an exceptionally fruitful area for development of new quantum materials, applying the exquisite structure control and ability to fine-tune unit cell sizes of, for example, unique, non-centrosymmetric structures accessible by BCP SA to emergent properties in correlated electron systems. However, the synthesis of high-quality quantum materials (e.g., superconductors) is extremely limited by the constraints of crystal growth inside mesoporous materials. In short, conventional solid-state thermal processing requires operation in a narrow window of temperature and time so as to produce the phase of interest without growth of crystalline domains beyond the boundaries of the mesostructure, which results in structural collapse.[23] While methods such as addition of a support framework[13] or directional recrystallization may extend the processing window, the realization of mesostructured quantum materials via BCP structure direction requires careful selection of the material of interest and optimization of its synthetic conditions. In superconductors in particular, the only study to date[22] produced niobium oxynitrides on the edge of mesostructure collapse and with T_cs of ≈8 K, less than half the best reported bulk niobium nitride (NbN) value. Here we describe the discovery of synthetic routes to niobium nitrides and carbonitrides with unusual structure retention even at temperatures as high as 1000 °C and resulting superconducting transition temperatures (T_c) comparable to their bulk analogues (the highest observed T_c in this study was 16 K, as compared with literature reports of 16.11 K in magnetron sputtered NbN[24] and 18 K in NbCN at optimal stoichiometric ratio[25]). We further demonstrate the full potential of soft BCP SA approaches in quantum material mesostructure control by producing four different mesostructures from a single block copolymer. Finally, we show first evidence for emergent quantum behavior in the form of mesostructure-T_c correlations and atypical flux avalanches in the resulting materials.

In this work, we develop a series of synthetic routes (**Figure 1**) to mesostructured niobium carbonitrides based on BCP SA, which overcomes the severe limitations of the previous route to niobium nitrides.[22] Briefly, a triblock terpolymer poly(isoprene-*b*-styrene-*b*-ethylene oxide), or ISO (86 kDa, volume fractions of 29% PI, 64% PS, 7% PEO, and dispersity of 1.09), was used to structure direct sol–gel-derived niobium (V) oxide nanoparticles into the alternating gyroid morphology. The resulting polymer–inorganic hybrid was calcined at 450 °C in air to remove the polymer, and then nitrided at 700 °C for 12 h in flowing ammonia gas to produce a niobium oxynitride of the approximate formula $NbN_{0.55}O_{0.45}$. This oxynitride was subsequently subjected to one of four gas treatments: either an additional anneal at 865 °C for 3 h in NH_3 (as in ref. [22]), 865 °C for 3 h in argon, 865 °C for 3 h in forming gas (5% H_2 in N_2) to produce a reduced nitride, or at up to 1000 °C for 3 h in carburizing gas (16/4/80 vol% $CH_4/H_2/N_2$) to produce a carbonitride or carbide.

The resulting materials were first characterized using X-ray diffraction/wide-angle X-ray scattering (XRD/WAXS) to probe their transformation into the desired atomic structures

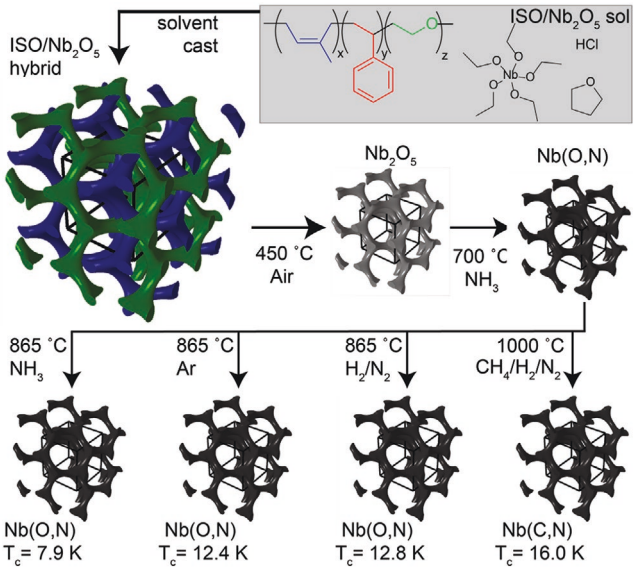

Figure 1. Synthetic routes to alternating gyroid mesostructured nitride and carbonitride superconductors. Please note that, upon first higher temperature processing at 450 °C, only one of the two gyroid minority network domains survives, that is, the one swollen with inorganic (here the green volume in the upper left alternating gyroid rendering). Variation of the final gas annealing step changes the T_c of the resulting material by a factor of 2 (see main text).

(**Figure 2**B, **Table 1**). Interestingly, annealing in inert gas (Ar), which originally occurred due to a serendipitous error, results in a higher lattice parameter (typically associated with higher N/O ratio) than annealing in ammonia (4.363 Å vs 4.318 Å). This observation can be understood in the context of a material of the form $NbN_xO_y[]_{1-x-y}$, where [] denotes vacancies. The vacancy concentration stems from kinetic trapping of vacancy states in the lattice during transformation, with an equilibrium limit associated with the oxidation state of the Nb centers in the lattice.[26] Annealing in high-purity argon, rather than in ammonia, does not involve reactive processes and allows the material to equilibrate at a lower overall vacancy concentration. Even more interestingly, the coherent scattering domain size of the sample annealed in argon (10 nm) is lower than that of the superconducting sample re-annealed in ammonia (12 nm). This result, while prima facie counterintuitive, is expected in the context of the driving forces for crystal growth. Using the conventional wisdom that bulk diffusion contributes to domain growth at $T > 0.5T_m$, one would not expect bulk crystal growth from temperature alone until about 1150 °C. The observed and substantial crystal growth in the 865 °C ammonia re-annealing step is thus likely a product of reactive re-precipitation of nitride, rather than thermal crystal growth. This is supported by a previous study of BCP-derived nitride synthesis[22] which showed that the annealing temperatures around which structures collapse vary only slightly with BCP molar mass (≈confinement length scale). If thermal crystal growth alone were the origin of structure collapse, one would expect more significant structural dependence of the necessary processing temperature. Therefore, solid-state reactions with a lower tendency toward recrystallization may result in less grain growth. To further probe this hypothesis, we annealed the starting nitride in forming gas

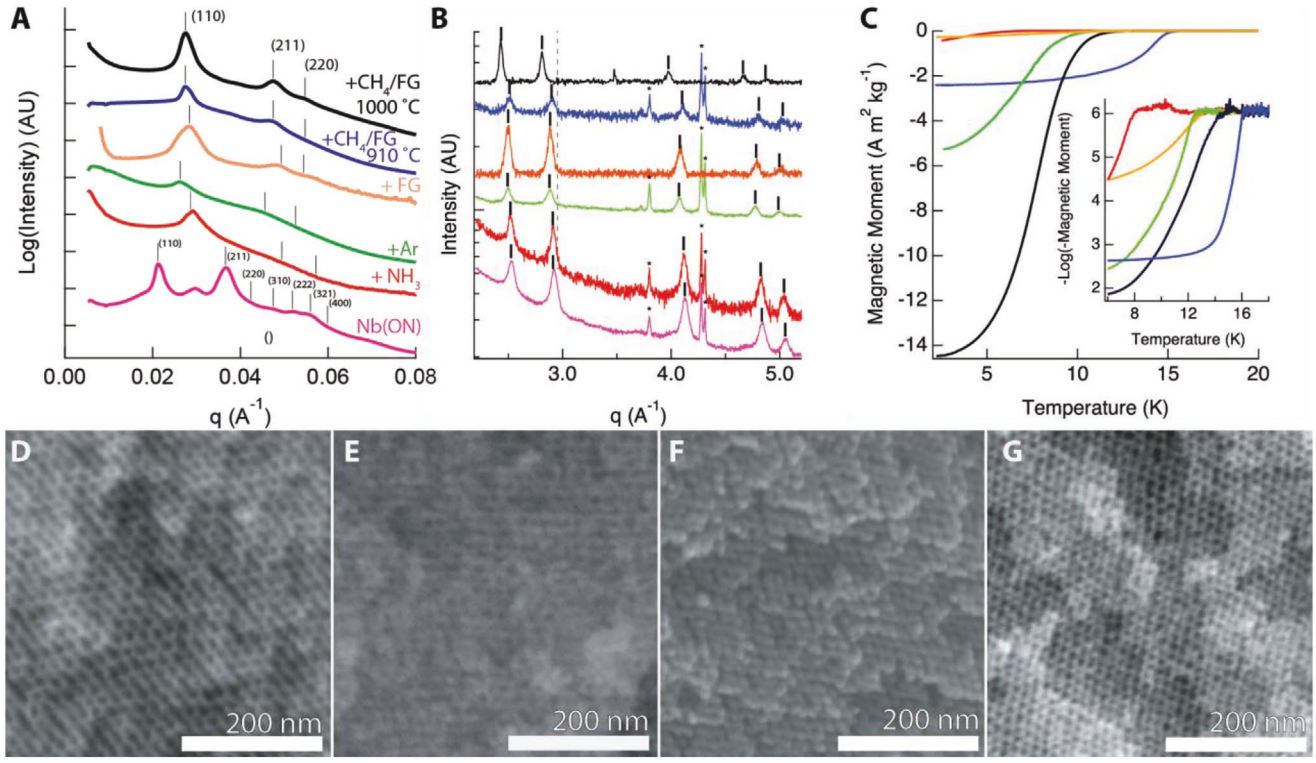

Figure 2. Structural investigation of the block-copolymer-directed superconductors shown in Figure 1. A) Synchrotron SAXS and B) powder XRD/WAXS of starting nitride treated at 700 °C (bottom) and re-annealed nitrides treated at 865 °C in (bottom to top) ammonia (red), argon (green), or forming gas (orange), at 910 °C in dilute carburizing gas (blue, see Experimental Section), and at 1000 °C in carburizing gas (black). In the SAXS patterns, | denotes peaks consistent with a $I4_132$ structure (space group #214) with lattice parameters as given in Table 1. In the WAXS patterns, | denotes peaks consistent with the NaCl type structure (lattice parameters given in Table 1), while * denotes instrument background peaks. The dashed vertical line in (B) just below 3 $Å^{-1}$ reflects the position of the (200) peak of the starting material, as a guide to the eye for peak shift in subsequent samples. C) Temperature-dependent magnetization curves of samples re-annealed at 865 °C in (red) ammonia, (green) argon, (orange) forming gas, (black) carburizing gas, and (blue) dilute carburizing gas. D–G) SEM images suggesting different degrees of structure preservation in the starting nitride (D) and samples re-annealed at 865 °C in ammonia (E) or forming gas (F) and at 1000 °C in carburizing gas (G).

(FG), which should more fully reduce the niobium and also exhibit limited grain growth. As expected, the lattice parameter shifted toward the lower-vacancy or higher-nitrogen direction (4.355 Å), consistent with reduction of the material, while the domain size (10 nm) remarkably again does not differ significantly from the starting material (8 nm), consistent with the hypothesis.

During these studies, we also annealed the starting material in carburizing gas at temperatures of 910 °C and 1000 °C, again first due to a serendipitous error. Remarkably, the material treated at 1000 °C had a lattice parameter (4.417 Å) near that expected for a pure NbC material, despite a domain size of just 9 nm. Further experiments confirmed that temperature variation produced a series of lattice parameters with minimal grain growth up to 1000 °C, though at 1100 °C the grains grew substantially and the mesostructure was lost (Figure S1, Supporting Information). We suspect that given the thermally activated nature of grain growth, this variation of processing capability with annealing temperature at the highest temperatures studied is associated with melt-driven grain growth, vide supra. This is consistent with exponential dependence of diffusivity and reaction rate consistent with a thermally activated

Table 1. Structural parameters of treated materials.

Gas treatment	Lattice parameters [Å]	Coherent scattering domain size [nm]	Mesostructure ($I4_132$) d_{100} [nm]	T_c (onset, [K])
Starting material – 700 °C/12 h	4.308 Å ± 0.001 Å	8 nm	42.0 nm	N/A
+865 °C/3h in NH_3	4.318 Å ± 0.002 Å	12 nm	30.5 nm	7.9 K
+865 °C/3h in Ar	4.363 Å ± 0.002 Å	10 nm	33.8 nm	12.4 K
+910 °C/3h in H_2/N_2	4.355 Å ± 0.001 Å	10 nm	31.3 nm	12.8 K
+910 °C/3h in $CH_3/H_2/N_2$	4.333 Å ± 0.003 Å	8 nm	32.1 nm	14.2 K
+1000 °C/3h in $CH_3/H_2/N_2$	4.417 Å ± 0.001 Å	9 nm	32.2 nm	16.0 K

process, as seen in other studies of block-copolymer-derived nitrides.[22,23]

To relate the Debye–Scherrer domain size results from WAXS with mesostructure retention, we used small-angle X-ray scattering (SAXS) to directly probe the degree of mesostructural order (Figure 2A, Table 1). All samples subjected to thermal treatment showed a general loss of higher-order SAXS peaks typical of high-temperature processing of ordered mesoporous ceramics, but the detrimental impact on long-range order was not equal for all processing conditions. Indeed, consistent with the WAXS results, the samples treated in Ar, but particularly in FG and carburizing gas, had dramatically better retention of the mesostructure than their NH_3-treated oxynitride analogues. This is shown by the presence of a second-order SAXS feature in the Ar- and FG-treated nitrides (green and orange traces in Figure 2A, respectively; consistent with the (211) family of diffraction peaks in the alternating gyroid) and the clear presence of second- and even third-order reflections in the carbides/carbonitrides (blue and black traces), contrasted with the weak single reflection in the NH_3-treated oxynitride (red trace).

To correlate the measured lattice parameters to superconducting properties, we used vibrating sample magnetometry (VSM, Figure 2C, Table 1). Strikingly, the Ar-treated sample exhibited an onset T_c of 12.4 K (Figure 2C, inset) and flux exclusion nearly two orders of magnitude greater than the previous best-in-class NH_3-treated sample.[22] Interestingly, despite a slightly higher T_c of 12.8 K, the FG-treated sample had flux exclusion comparable to that of the original nitride. The carbonitride/carbide samples exhibited both strikingly enhanced flux exclusion (comparable to the Ar-treated nitride) and T_c as high as 16K, approaching the best literature reports for the pure NbN system[24] and within a few degrees of the best reported for the Nb–C–N pseudobinary alloys.[25] The observed variation in T_c may be related primarily to the composition of the material (O/N ratio, vacancy concentration, and Nb oxidation state), while the flux exclusion may be related to the superconducting fraction of the material or to other inherent material properties.

Finally, to confirm the mesostructure retention in real space, we used scanning electron microscopy (SEM, Figure 2D–G). Consistent with the WAXS and SAXS results, the structure in the ammonia-treated nitride (Figure 2E) was noticeably degraded from the starting material, (Figure 2D) while the forming-gas-treated nitride (Figure 2F) had a markedly better-preserved structure and the carbide (Figure 2G) had a structure comparable to that in the starting material.

We speculate that the remarkable quality of the structure retention in the carbonitrides is due to the multistep pathway involved in production of active gas-phase species from methane as compared to ammonia. Ammonia is known to readily degrade to N and H radical species at temperatures above 700 °C,[27] while methane degradation follows complex, multistep pathways.[28] It stands to reason that these pathways may produce a strikingly lower concentration of active carbon species (ACS) in a CH_4-based gas blend when compared with NH_3, particularly considering that the presence of a carrier gas and H_2 likely shifts the degradation equilibrium for CH_4 to favor even lower ACS concentration. This low concentration of ACS results in a low rate of nitride–carbide conversion as compared to the rate of oxynitride–nitride conversion, resulting in less crystal growth at a given temperature and a dramatically increased maximum processing temperature, from 865 °C to over 1000 °C (vide supra). The ability to process the material at such high temperatures enables yet-unachieved levels of both mesostructure retention and electronic material quality in mesostructured superconductors.

To demonstrate the versatility of this BCP-directed synthetic pathway, we used a single parent ISO terpolymer to prepare samples with different characteristic morphologies based on a theoretical description of the phase behavior of the ISO triblock terpolymer[29] (**Figure 3**A). Addition of increasing amounts of oxide nanoparticle sol to the same amount of ISO in solution, upon solvent evaporation is expected to selectively swell the PEO (O) block of ISO more and more with inorganic material.[30–33] For the particular ISO composition used here, this is analogous to moving upward along the white isopleth of the ISO terpolymer phase diagram shown in Figure 3A. Indeed, with increasing amount of oxide sol, the following four morphologies were obtained: The alternating gyroid ($I4_132$, Figure 3N), the perforated lamellar phase (layer group $P\overline{1}$, Figure 3J), the double gyroid ($Ia\overline{3}d$, Figure 3F), and the inverse hexagonally packed cylinder phase (P6mm, Figure 3B). It should be noted that the phase diagram in Figure 3A is a simulation for a neat ISO triblock without additives. The addition of oxide sol would, at a minimum, change the pair-component χN values dramatically, with further effects at the high-PEO end of the phase diagram including particle-induced polymer conformation changes. With that said, one would expect the general sequence of phases to remain comparable, consistent with other literature observations.[31,34] The resulting materials' mesostructure retention was characterized at all processing stages by SAXS: as-made material, calcined at 450 °C in air, nitrided at 700 °C for 12 h in flowing ammonia gas, and after an additional heat treatment at 1000 °C for 3 h in carburizing gas (Figure 3Q,M,I,E; and Figures S2A, S3A, S4A, and S5A, Supporting Information; from bottom to top: hybrid (red), oxide (blue), nitride (green), and carbide (black)). In all cases, the relative positions of the peaks remain consistent, indicating morphology retention through the various heat treatments, while the main peak position gradually shifts to higher q, indicating shrinkage of the mesostructure in all cases except for lamellae. In the alternating gyroid nitride (Figure 3Q, green trace) and in the double-gyroid oxide (Figure 3I, blue trace), unexpected SAXS peaks are observed at $q/q^* = \sqrt{4}$ and $\sqrt{2}$, respectively. Such features typically originate from symmetry breaking due to anisotropic compression of the lattice as often occurs during thermal processing of refractory nitrides.[35] Mesostructure retention is confirmed by SEM of the starting oxide (Figures S2B, S3B, S4B, and S5B, Supporting Information), the intermediate (700 °C) nitrides (Figure 3O,K,G,C; Figures S2C, S3C, S4C, and S5C, Supporting Infrmatin) and the final (1000 °C) carbides (Figure 3P,L,H,D; Figures S2D, S3D, S4C, and S5C, Supporting Information), which show characteristic projections for each morphology.

In the case of the lamellae, closer inspection of SEM images suggests the presence of ordered perforations between the lamellar sheets (Figure 3K,L; Figure S6, Supporting Information). This observation is corroborated by the presence of a peak for the hybrid (and oxide; red/blue traces, peak position

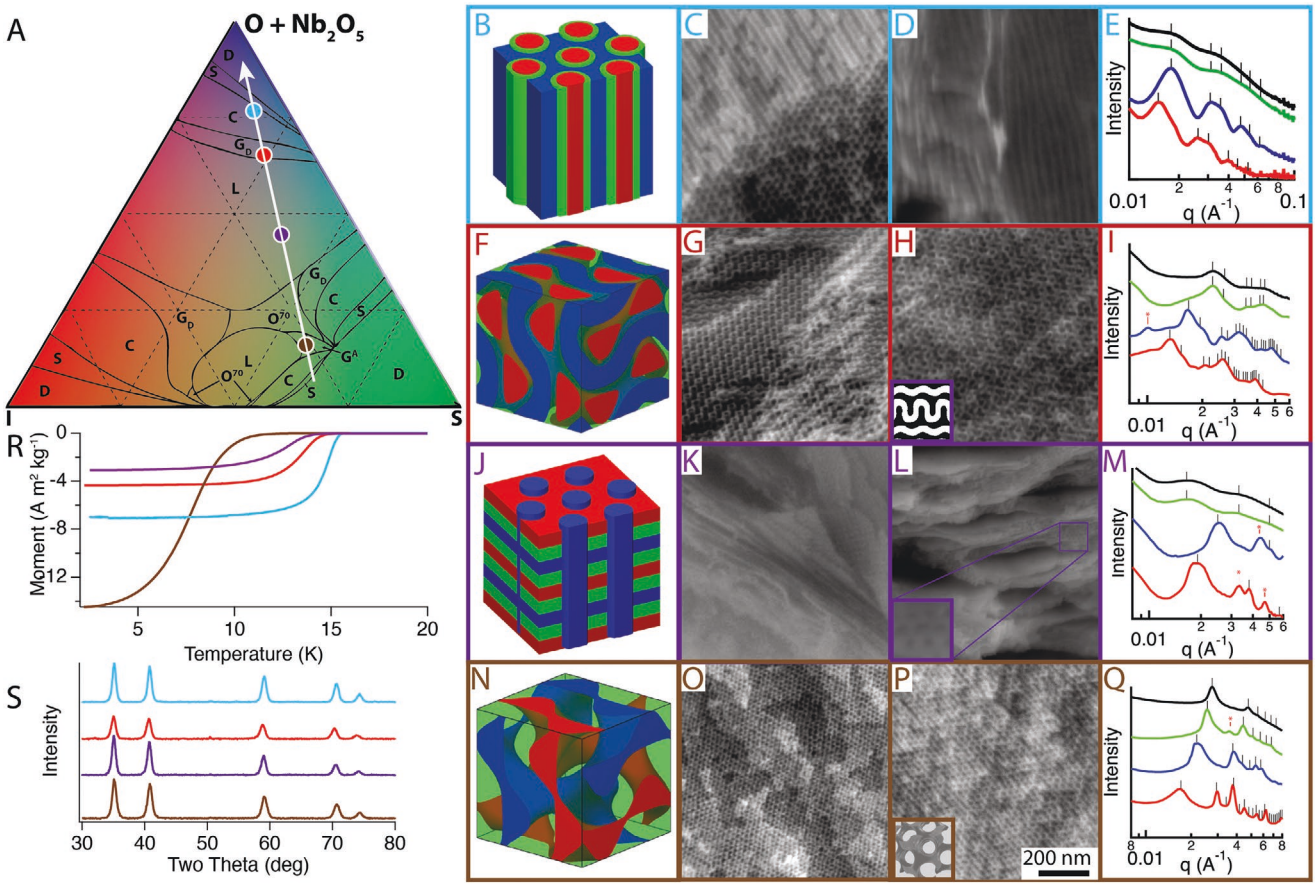

Figure 3. Morphology control of BCP-SA-directed superconductors. A) Simulated phase diagram for isoprene-*b*-styrene-*b*-ethylene oxide (ISO) triblock terpolymers as a guide to the expected phase behavior of the parent polymer. The isopleth highlighted by the white line corresponds to compositions of ISO-83 terpolymer + inorganic used here, with the base of the isopleth at the neat polymer volume fractions and the brown, purple, red, and teal markings indicating the compositions of the alternating gyroid, lamellar, double-gyroid matrix, and hexagonal morphologies, respectively. It should be emphasized that this phase diagram is merely a guide to the expected sequence of morphologies in the parent polymer, and not a representation of the phase behavior of the polymer/oxide composite system. A) Adapted with permission.[29] Copyright 2007, American Chemical Society. B,F,J,N) Renderings of the target morphology, where the dark blue color represents the (hybrid) PEO + Nb_2O_5 domain retained as pure inorganic domain during thermal processing. C,G,K,O) SEM images of 700 °C heat-treated nitrides showing four different morphologies. G,H) The (211) "double-wavy" projection of the double gyroid and O,P) the sixfold symmetry characteristic of the (111) projection of the alternating gyroid. The insets in (H,P) show the calculated projection along the given axis, while an inset in (L) highlights an area of sixfold symmetry consistent with hexagonal perforations. D,H,L,P) SEM images of 1000 °C heat-treated carbides demonstrating morphology retention. E,I,M,Q) Small-angle X-ray scattering (SAXS) patterns for each of the four morphologies as they progress through heat treatments, from bottom to top in each frame: polymer–oxide hybrid (red), freestanding oxide (blue), nitride (green), and carbide (black). The ticks indicate the expected peak positions for the targeted mesoscale lattice with resulting lattice parameters summarized in Table 2, while the red ticks with asterisks indicate peaks inconsistent with the assigned lattice; in (M), these peaks likely originate from a hexagonal sublattice while in (I,Q), the features likely originate from anisotropic compression of the structure. R) Temperature-dependent magnetization of structured carbides showing a morphology-dependent superconducting transition at temperatures between 12 and 16 K. S) Wide-angle X-ray diffraction patterns of structured carbides consistent with the phase-pure rocksalt NbC structure.

indicated by red*|) at approximately 0.031 $Å^{-1}$, a position not consistent with an expected lamellar reflection but consistent with hexagonal order ($q/q^* = \sqrt{3}$). Generally, lamellar mesostructures cannot survive removal of non-inorganic components containing block copolymer domains with retention of mesoscale porosity due to material collapse. The presence of these perforations may explain why the material is able to retain mesoscale structure despite heating to 1000 °C. The very weak low-angle features observed in the SAXS patterns for the nitride and carbide likely also originate from this hexagonal sublattice.

XRD was used to verify the production of the carbide phase (Figure 3S; Figure S7, Supporting Information). Consistent with the results from the single-morphology studies, in all cases the carbide was prepared without significant impurity phases. The carbide lattice parameters and coherent scattering domain sizes are summarized in **Table 2**, and the diffraction patterns for the intermediate nitrides are given in Figure S7, Supporting Information.

Finally, to verify that the ordered carbides were superconducting, we again used VSM (Figure 3R). All four morphologies exhibited a superconducting transition with a high flux exclusion consistent with that of the carbides studied earlier. Remarkably, the samples of different morphology exhibited transition temperatures varying systematically with oxide

Table 2. Lattice parameters and domain sizes for nitrides and carbides.

Morphology	Processing stage	Lattice parameter [Å]	Coherent scattering domain size [nm]	T_c (onset, [K])
Alternating gyroid	Nitride	4.311 Å ± 0.009 Å	7.6 nm	N/A
Alternating gyroid	Carbide	4.417 Å ± 0.004 Å	9.2 nm	14.2 K
Perforated lamellae	Nitride	4.296 Å ± 0.023 Å	7.4 nm	N/A
Perforated lamellae	Carbide	4.427 Å ± 0.004 Å	10.4 nm	15.3 K
Double gyroid	Nitride	4.323 Å ± 0.010 Å	8.2 nm	N/A
Double gyroid	Carbide	4.437 Å ± 0.004 Å	9.6 nm	15.5 K
Hexagonal cylinders	Nitride	4.314 Å ± 0.011 Å	8.7 nm	N/A
Hexagonal cylinders	Carbide	4.420 Å ± 0.003 Å	10.8 nm	16.0 K

loading in the starting hybrid from 14.2 K in the alternating gyroid to 16.0 K in the hexagonal cylinders. This result would not be unexpected given the highly surface-sensitive nature of the solid-state reaction, but it is curious that the transition temperatures vary without substantial and systematic variation of the XRD-measured lattice parameters (see Table 2). While the coherence length for Cooper pairs in these materials (upper limit of ≈7 nm for pure NbN single crystals[36]) is much smaller than the unit cell size of the mesoscale lattice (≈30 nm, vide infra), making direct interaction between the superconducting pairing and the lattice unlikely, the correlation in the absence of systematic lattice parameter shifts suggests that the variation may be due to an inherent size- or morphology-related effect, rather than processing-induced compositional variations. Comparison of the strut thickness (derived from volume fractions and SAXS-measured lattice parameters) and the T_c suggests a correlation but is inconclusive (Figure S8, Supporting Information).

Based on this unexpected morphology-T_c correlation, the field-dependent magnetization of the double-gyroid sample (red box in Figure 3) was measured at a temperature of 2 K (≈0.129T_c, **Figure 4**, red trace). In contrast to field-dependent magnetization measurements at 7 K (≈0.5T_c), which have a typical hysteretic behavior characteristic of type II superconductors, the 2 K measurement exhibits abrupt jumps in the magnetization during the field sweep. These jumps are comparable in overall behavior to flux avalanches,[9,37] but have several striking differences. First, the avalanches occur at incoherent, but uniform spacing from very low field (≈7.95×10^4 A m^{-1}, 1 kOe) to the highest field measured (≈3.18×10^6 A m^{-1}, 40 kOe). Second, the avalanches have nearly constant beginning and ending magnetizations. Finally, the magnitude of the magnetization remains relatively constant throughout the entire region scanned. Interestingly, this behavior occurs only on samples prepared within ≈6 h of measurement (i.e, less than 6 h elapsed between removal from the CH_4 annealing tube and insertion into the PPMS vacuum chamber). Curiously, samples held in sealed, air-filled vials for ≈1 week exhibited this atypical avalanche behavior at lower temperatures/fields, and samples held for longer times had standard magnetic response, suggesting that the behavior is highly sensitive to oxidation of the nitride surface.

While definitively or even conclusively assigning such an incoherent behavior to a physical phenomenon would require extensive modeling which may still not fully describe the behavior in this polycrystalline sample, we believe that these three atypical features suggest a balance between the critical current and thermal conductivity of the material consistent with an interpretation of the thermomagnetic (TM) model for flux avalanche initiation and propagation in a porous, bulk solid.[38,39] In brief, the TM model describes flux jumps resulting from local Joule heating of the superconductor at a defect site coupled with slow heat transfer out of the material due to a very low temperature (where phononic, rather than electronic, heat conduction modes dominate[40]) and the material geometry, porosity, and properties. Similarly, theoretical and experimental studies of granular superconductivity support magnetization behavior qualitatively similar to observations in our materials.[41,42] Briefly, in granular superconductors, a difference of several orders of magnitude in critical current density between particles and a matrix drives the formation of hypervortices spanning several grains. A peak corresponding to a critical field for intragranular motion of a hypervortex can

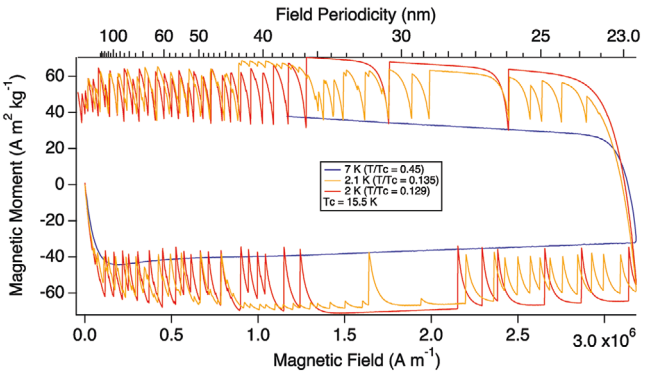

Figure 4. Atypical flux avalanche behavior in gyroidal carbonitrides. Field-dependent magnetization of a double-gyroid matrix carbonitride showing high-field flux avalanches. The red and orange traces are successive measurements on the same sample, showing that the position of the flux jumps is not systematically reproduced, while the blue trace represents the same sample at temperatures closer to T_c. It should be noted that the additional avalanche behavior represents additional flux expulsion over and above the higher-temperature behavior; the jumps are consistent with local quenching back to the high-T state. The top axis reflects the field in units of the density of magnetic flux quanta at that field. The relative stabilization as the field matches the mesoscale repeat between 9.5×10^5 A m^{-1} (14 kOe) and 2.2×10^6 A m^{-1} (28 kOe) suggesting flux pinning on the mesoscale lattice. Note that 1 A m^{-1} = 4π / 10^3 Oe; A m^{-1} is the SI unit of magnetic field. The direction for all scans is counterclockwise in the plot.

then be observed in the magnetization curve. The dramatically decreased thermal conductivity in these samples combined with the low measurement temperature in and of itself may be expected to lead to a conventional TM avalanche behavior, and similar mesostructured niobium oxynitrides are known to have spatial variations in observed lattice parameter consistent with compositional inhomogeneity as might be expected to lead to granular superconductivity.[22] We note that the flux avalanches are smaller in magnitude, lower in frequency, or non-existent between $\approx 9.55 \times 10^5$ A m^{-1} (12 kOe) and $\approx 2.23 \times 10^6$ A m^{-1} (28 kOe), a field range which corresponds to a spacing between flux quanta of 28 to 45 nm, which is comparable to the projected pore-to-pore spacing of the alternating gyroid in this sample. It is interesting to note that this stabilization is consistent even at slightly different measurement temperature (orange trace, Figure 4). It is important to note that this spacing will vary not only from grain to grain due to polydispersity of the sample, but also with orientation of any particular grain relative to the magnetic field. The realization of bulk single mesocrystals of such superconductors, coupled with modeling, may provide a more full description of this emergent behavior.

Despite substantial promise for the realization of yet-unexplored structure–property correlations, the convergence of block copolymer–inorganic hybrid co-assembly and quantum materials (e.g., correlated electron systems) remains elusive. This gap is largely due to a lack of synthetic approaches to produce mesostructured, electronic-grade materials from block copolymers. In this work, we used systematic variation of high-temperature annealing conditions to discover a route to niobium carbonitrides from block-copolymer-directed niobium oxides and nitrides. The resulting materials have superconducting transition temperatures as high as 16 K, doubling the previous record for block-copolymer-directed mesoporous superconductors. To demonstrate the robust, tunable nature of this approach, we synthesized four different periodically ordered morphologies from a single parent triblock terpolymer. Remarkably, the T_c of the materials varies systematically with the overall oxide loading, suggesting a confinement- or mesostructure-driven effect, and the double-gyroid sample exhibits flux jumps/avalanches with local stabilization possibly consistent with local increase of the critical current at fields where the spacing between flux quanta matches that of the porous mesostructure. We expect that this design strategy for superconductors with controlled, high quality mesoscale order will prove to be a robust platform for studies of mesostructure-property correlations in superconductors and other quantum materials.

Experimental Section

Materials: All reagents were purchased from Sigma–Aldrich and used as received unless otherwise noted. Benzene was purchased from TCI America and vacuum-distilled from n-butyllithium before use. Isoprene and styrene were vacuum-distilled from n-butyllithium and calcium hydride, respectively, before use. Tetrahydrofuran (THF, inhibitor free) used for polymer synthesis was purchased from Fisher Scientific and vacuum-distilled from n-butyllithium before use. Methanol and chloroform were purchased from Avantor Performance Materials. THF for evaporation induced self-assembly was purchased from Sigma–Aldrich and used as received. Hydrochloric acid (37% by mass in water) was purchased from Fisher Scientific. Niobium (V) ethoxide (99.999% atomic fraction, metals basis) was purchased from Alfa Aesar. Ammonia (electronic grade, 99.9995% by mass) was purchased from Matheson Tri-Gas or Praxair based on availability; no differences were observed between the two suppliers. Argon (ISP grade), forming gas (certified standard), carburizing gas (certified standard), and air (Ultra Zero grade) were purchased from Airgas.

Polymer Synthesis: The poly(isoprene-*b*-styrene-*b*-ethylene oxide) (ISO) triblock terpolymer used was synthesized by sequential anionic polymerization using known techniques.[34,43] In brief, isoprene polymerization was initiated in benzene by sec-butyllithium. Styrene was then added after at least 8 h. After at least another 8 h, one molar equivalent of ethylene oxide gas was double-distilled and added, followed by termination of the polymer with methanolic HCl. The resulting methoxy-terminated poly(isoprene-*b*-styrene) was redissolved in chloroform, washed with water, and precipitated into cold methanol before drying for at least 5 days at 130 °C on a high vacuum line. THF was then vacuum-distilled onto this polymer, which was re-initiated with potassium napthalenide before the addition of a predetermined amount of ethylene oxide monomer. Termination, washing, and precipitation steps were then repeated as for the diblock precursor and the resulting ISO characterized by a combination of size exclusion chromatography (GPC) and ^{1}H nuclear magnetic resonance (NMR) spectroscopy. The polymer had a dispersity of 1.09 and an overall molar mass of 86 kDa with volume fractions of 29.4% PI, 64.1% PS, and 6.5% PEO. These volume fractions assume block densities of 0.83 g cm^{-3} for PI, 0.97 g cm^{-3} for PS, and 1.06 g cm^{-3} for PEO.

Mesoporous Niobium (V) Oxide and Niobium Oxynitride Synthesis: The ISO triblock terpolymer was used to prepare mesostructured niobium (V) oxide and niobium nitride following previously reported procedures.[15] Briefly, a stock solution of Nb_2O_5 sol nanoparticles was prepared via an acid-catalyzed sol–gel method in THF. Predetermined amounts of the stock solution were added to the solutions of the block copolymer (polymer-to-THF ratio of 75 mg/2 mL) to give the desired morphology: 0.247 mL for the alternating gyroid strut samples shown in Figure 2 and Figure 3O,P,Q; 0.401 mL for the perforated lamellar samples shown in Figure 3K,L,M; 0.958 mL for the double-gyroid matrix samples shown in Figure 3G,H,I; 1.058 mL for the hexagonal cylinders samples shown in Figure 3C,D,E. Volume fractions shown in Figure 3A were determined by assuming complete incorporation of the sol–gel oxide into the final nanocomposite and assuming an oxide component density of 2 g cm^{-3} for the alternating gyroid sample and 0.52 g cm^{-3} for all other samples in the hybrid state. These densities were dramatically lower than the literature value of 4.6 g cm^{-3} for bulk Nb_2O_5,[44] but well within the expected range taking into account the porosity of fractal aggregates.[45] The alternating gyroid density was established based on previous studies of ISO + Nb_2O_5 sol–gel co-assembly.[34] We suspect that the shifted, lower density needed to match simulation phase behavior at high oxide loading reflects a combination of a shift in the effective Flory–Huggins interaction parameter of the PEO + oxide phase with the other components at high oxide loadings. For comparison, we also plotted the same phase diagram (Figure S9, Supporting Information) using a uniform density of 2.0 for all points on the phase diagram. As expected, the points disagree with the simulation-derived neat polymer phase diagram, an outcome consistent with that of points also plotted for a previous ISO + Nb_2O_5 study employing the same oxide component density.[34] After sol addition, the solutions were allowed to evaporate under a glass dome at 35 °C until dry. The resulting films were then annealed at 130 °C under vacuum. The block copolymer was then removed by calcination at 450 °C for 3h (heating ramp rate 1 °C min^{-1} and ambient cooling) to give freestanding oxide. These oxides were then treated in flowing ammonia gas at 700 °C for 12 h (heating ramp rate 5 °C min^{-1} and cooling 25 °C min^{-1}) to give a niobium oxynitride.

Solid State Synthesis: The reactions described in the lower third of Figure 1 were performed in a Lindberg model 55035 tube furnace equipped with a custom gas switching manifold and 1" quartz tube. The sample to be treated was placed in a quartz crucible (Technical

Glass Products) and the tube ends sealed to the gas system. For the different syntheses, the different gases (ammonia, argon, forming gas, carburizing gas) were flowed during the entire duration of furnace heating and cooling at 10 L h^{-1}. The sample prepared in dilute carburizing gas was prepared just after changing the manifold (with an internal volume of ≈10 L) from forming gas to carburizing gas, retaining a plug of forming gas that slowly diluted the methane component of the carburizing gas during the anneal. The remarkable performance of this one-off sample could not be reproduced due to a lack of quantitative gas blending capability on the system, but demonstrates one example of an optimized result that may result from further systematic exploration of the Nb(C–N–O) pseudo-ternary system. After cooling, argon was flowed over the sample at a rate of 20 L hr^{-1} for 2 h, followed by flowing dry air at a rate of 20 L h^{-1} for 1 h. This final step was intended to controllably grow a dense surface oxide layer rather than a porous layer, which may form on exposure to humid air during sample removal. After synthesis, samples were stored in a nitrogen-purged, light-free dessicator cabinet to minimize environmental degradation. No degradation was observed in samples stored in air, though systematic studies of this behavior were not undertaken.

Scanning Electron Microscopy: SEM images were captured using a Tescan Mira microscope operating at an accelerating voltage of 5 kV and using an in-lens secondary electron detector. Samples were fractured on carbon tape and sputter coated with Au–Pd to reduce charging prior to imaging. Strut thicknesses determined via SEM were measured by taking multiple line-cuts of SEM images and averaging the width of 20–30 visible struts in a given image. Renderings of gyroid cross-sections in Figure 3; and Figure S4, Supporting Information, were calculated using the CrossSectDensityPlot MATLAB program by Ethan Susca.

X-ray Diffraction: XRD/WAXS patterns were collected on either a Rigaku Ultima IV equipped with a Cu tube operated at 40 kV and 50 mA and a D/max Ultra strip detector, or a Bruker D8 Advance Eco equipped with a 1 kW Cu tube and a 160-channel Si strip detector. Scan rates were between 2° min^{-1} and 5° min^{-1} depending on the quantity of sample available and observed signal to noise ratio. Reported lattice parameters were determined by averaging Gaussian fits to the five observed peaks consistent with the rocksalt ($Fm\bar{3}m$) structure, with uncertainties determined from the standard deviations of fit of those peak positions. Coherent scattering domain sizes were determined using the Debye–Scherrer equation with a shape factor of 0.9 for the same five peaks.

Small-Angle X-ray Scattering: SAXS patterns were collected either at station G1 of the Cornell High Energy Synchrotron Source (CHESS; all patterns except the forming gas-treated sample in Figure 2B) or on a home-built beamline. The apparatus at CHESS consisted of a standard three-slit setup used to collimate the beam to a 0.25 × 0.25 mm rectangle, an evacuated sample-to-detector distance of typically 2 m, and a Dectris EIGER 1M pixel-array detector. The home-built setup consisted of a Rigaku rotating anode source, a set of orthogonal Franks focusing mirrors, a sample–detector distance of ≈88 cm, and a phosphor-coupled CCD described in detail elsewhere.[46] The 2D scattering patterns were converted to scattering vector **q** and radially averaged using the Nika software for Igor Pro.[47] For the alternating gyroid hybrid sample (red trace in Figure 3Q/S2), a substantial degree of texture was observed; to capture only reflections originating from a single grain, a ±15° sector was integrated around 309° from the horizontal, see Figure S10, Supporting Information.

Vibrating Sample Magnetometry: VSM data were collected using a Quantum Design Physical Property Measurement System equipped with a 9 T superconducting magnet and a liquid helium cryostat. Samples were mounted in polypropylene capsules inside a brass half-tube mounted on the VSM transport head and zero-field-cooled to 2 K. A small field of either 4000 A m^{-1} or 8000 A m^{-1} (50 Oe or 100 Oe) was applied and the sample position determined by scanning the transport through its travel. For temperature-dependent moment measurements, the sample was then warmed at 0.2 K min^{-1} while continuously measuring the magnetic moment until a temperature of 20 K was reached. The sample was then either warmed and removed or the field switched off and the sample re-cooled for further measurements. For field-dependent moment measurements, the field was returned to 0 A m^{-1} and then the field swept at a rate of 7960 A m^{-1} s^{-1} (100 Oe s^{-1}), with data from the VSM averaged in 0.1 s intervals. The field was swept uniformly from 0 to 3.18×10^6 A m^{-1} (40 000 Oe), where the magnet was left with a persistent field for ≈60 min while the system generated sufficient liquid helium to discharge the magnet. The field was then swept uniformly from 3.18×10^6 (40 000 Oe) to 0 A m^{-1}. In the replicate measurement, the sweep was stopped at approximately 2.63×10^6 A m^{-1} (40 000 Oe) due to low helium level.

Supporting Information

Supporting Information is available from the Wiley Online Library or from the author.

Acknowledgements

This work was funded by the National Science Foundation under award DMR-1707836 (to U.W.) and by the US Department of Energy under grant DE-SC0017631 (to S.M.G). P.A.B. was supported by the National Science Foundation (NSF) Graduate Research Fellowship Program under grant number DGE-1650441. This work made use of the Cornell High Energy Synchrotron Source (CHESS), which is supported by the NSF (DMR-1332208), and the Cornell Center for Materials Research (CCMR) shared facilities, which are supported by the NSF MRSEC program (DMR-1719875). The authors thank Jörg G. Werner for kind assistance with graphics and Ethan M. Susca for helpful discussions. Certain commercial equipment, instruments, materials, suppliers, or software are identified in this paper to foster understanding. Such identification does not imply recommendation or endorsement by the National Institute of Standards and Technology, nor does it imply that the materials or equipment identified are necessarily the best available for the purpose.

Conflict of Interest

The authors declare no conflict of interest.

Data Availability Statement

The data that support the findings of this study are available from the corresponding author upon reasonable request.

Keywords

block copolymers, mesostructured materials, quantum metamaterials, self-assembly, superconductors

Received: October 13, 2020
Revised: February 17, 2021
Published online:

[1] L. R. Meza, S. Das, J. R. Greer, *Science* **2014**, *345*, 1322.
[2] K. Hur, Y. Francescato, V. Giannini, S. a. Maier, R. G. Hennig, U. Wiesner, *Angew. Chem., Int. Ed.* **2011**, *50*, 11985.
[3] M. Fruchart, S.-Y. Jeon, K. Hur, V. Cheianov, U. Wiesner, V. Vitelli, *Proc. Natl. Acad. Sci. USA* **2017**, *115*, E3655.
[4] K. Hur, R. G. Hennig, U. Wiesner, *J. Phys. Chem. C* **2017**, *121*, 22347.

[5] M. Maldovan, E. L. Thomas, *Periodic Materials and Interference Lithography for Photonics, Phononics and Mechanics*, Wiley-VCH, Weinheim, Germany **2009**.
[6] J. K. Yu, S. Mitrovic, D. Tham, J. Varghese, J. R. Heath, *Nat. Nanotechnol.* **2010**, *5*, 718.
[7] E. Bousquet, M. Dawber, N. Stucki, C. Lichtensteiger, P. Hermet, S. Gariglio, J.-M. Triscone, P. Ghosez, *Nature* **2008**, *452*, 732.
[8] L. Piraux, X. Hallet, *Nanotechnology* **2012**, *23*, 355301.
[9] M. Motta, A. V. Silhanek, W. A. Oritz, in *Oxford Handbook of Small Superconductors* (Ed: A.V. Narlikar), Oxford University Press, Oxford, UK **2018**, pp. 379–414.
[10] N. I. Zheludev, *Science* **2010**, *328*, 582.
[11] A. M. Zagoskin, *J. Opt.* **2012**, *14*, 114011.
[12] M. Templin, *Science* **1997**, *278*, 1795.
[13] J. Lee, M. Christopher Orilall, S. C. Warren, M. Kamperman, F. J. DiSalvo, U. Wiesner, *Nat. Mater.* **2008**, *7*, 222.
[14] P. D. Yang, D. Y. Zhao, D. I. Margolese, B. F. Chmelka, G. D. Stucky, *Nature* **1998**, *396*, 152.
[15] V. Z. H. Chan, J. Hoffman, V. Y. Lee, H. Iatrou, A. Avgeropoulos, N. Hadjichristidis, R. D. Miller, E. L. Thomas, *Science* **1999**, *286*, 1716.
[16] P. R. L. Malenfant, J. Wan, S. T. Taylor, M. Manoharan, *Nat. Nanotechnol.* **2007**, *2*, 43.
[17] K. W. Tan, B. Jung, J. G. Werner, E. R. Rhoades, M. O. Thompson, U. Wiesner, *Science* **2015**, *349*, 54.
[18] S. C. Warren, L. C. Messina, L. S. Slaughter, M. Kamperman, Q. Zhou, S. M. Gruner, F. J. DiSalvo, U. Wiesner, *Science* **2008**, *320*, 1748.
[19] Z. Li, K. Hur, H. Sai, T. Higuchi, A. Takahara, H. Jinnai, S. M. Gruner, U. Wiesner, *Nat. Commun.* **2014**, *5*, 3247.
[20] H. Y. Hsueh, Y. C. Huang, R. M. Ho, C. H. Lai, T. Makida, H. Hasegawa, *Adv. Mater.* **2011**, *23*, 3041.
[21] J. G. Werner, T. N. Hoheisel, U. Wiesner, *ACS Nano* **2014**, *8*, 731.
[22] S. W. Robbins, P. A. Beaucage, H. Sai, K. W. Tan, J. G. Werner, J. P. Sethna, F. J. DiSalvo, S. M. Gruner, R. B. Van Dover, U. Wiesner, *Sci. Adv.* **2016**, *2*, e1501119.
[23] P. A. Beaucage, E. M. Susca, S. M. Gruner, U. B. Wiesner, *Chem. Mater.* **2017**, *29*, 8973.
[24] S. P. Chockalingam, M. Chand, J. Jesudasan, V. Tripathi, P. Raychaudhuri, *Phys. Rev. B* **2008**, *77*, 214503.
[25] N. Pessall, R. E. Gold, H. A. Johansen, *J. Phys. Chem. Solids* **1968**, *29*, 19.
[26] R. Shipra, N. Kumar, A. Sundaresan, *Mater. Chem. Phys.* **2013**, *139*, 500.
[27] F. Schüth, R. Palkovits, R. Schlögl, D. Su, *Energy Environ. Sci.* **2012**, *5*, 6278.
[28] V. L. S. T. Silva, M. Schmal, S. T. Oyama, **1996**, *182*, 168.
[29] C. A. Tyler, J. Qin, F. S. Bates, D. C. Morse, *Macromolecules* **2007**, *40*, 4654.
[30] P. F. W. Simon, R. Ulrich, H. W. Spiess, U. Wiesner, *Chem. Mater.* **2001**, *13*, 3464.
[31] B. C. Garcia, M. Kamperman, R. Ulrich, A. Jain, S. M. Gruner, U. Wiesner, *Chem. Mater.* **2009**, *21*, 5397.
[32] T. N. Hoheisel, K. Hur, U. B. Wiesner, *Prog. Polym. Sci.* **2015**, *40*, 3.
[33] K. Hur, U. B. Wiesner, *Adv. Polym. Sci.* **2013**, *262*, 259.
[34] M. Stefik, S. Mahaian, H. Sai, T. H. Epps, F. S. Bates, S. M. Gruner, F. J. Disalvo, U. Wiesner, *Chem. Mater.* **2009**, *21*, 5466.
[35] S. W. Robbins, H. Sai, F. J. Disalvo, S. M. Gruner, U. Wiesner, *ACS Nano* **2014**, *8*, 8217.
[36] Z. H. Barber, D. M. Tricker, M. G. Blamire, *IEEE Trans. Appl. Supercond.* **1995**, *5*, 2314.
[37] I. A. Rudnev, D. V. Shantsev, T. H. Johansen, A. E. Primenko, *Appl. Phys. Lett.* **2005**, *87*, 042502.
[38] R. G. Mints, A. L. Rakhmanov, *Rev. Mod. Phys.* **1981**, *53*, 551.
[39] P. S. Swartz, C. P. Bean, *J. Appl. Phys.* **1968**, *39*, 4991.
[40] F. Koechlin, P. Dolegieviez, in *Proc. Fifth Workshop RF Superconductivity*, DESY, Hamburg, Germany **1991**, p. 463.
[41] V. K. Ignatjev, *Low Temp. Phys.* **1998**, *24*, 339.
[42] T. Scheike, W. Böhlmann, P. Esquinazi, J. Barzola-Quiquia, A. Ballestar, A. Setzer, *Adv. Mater.* **2012**, *24*, 5826.
[43] T. S. Bailey, C. M. Hardy, T. H. Epps, F. S. Bates, *Macromolecules* **2002**, *35*, 7007.
[44] S. Kuck, H. Werheit, *Non-Tetrahedrally Bonded Binary Compounds II* (Ed: O. Madelung), Condensed Matter, Springer-Verlag, Berlin, Germany **2000**, pp. 354–363.
[45] J. Gregory, *Water Sci. Technol.* **1997**, *36*, 1.
[46] M. W. Tate, S. M. Gruner, E. F. Eikenberry, *Rev. Sci. Instrum.* **1997**, *68*, 47.
[47] J. Ilavsky, *J. Appl. Crystallogr.* **2012**, *45*, 324.